Materials Horizons

ROYAL SOCIETY OF CHEMISTRY

COMMUNICATION

View Article Online
View Journal

Cite this: DOI: 10.1039/d3mh00270e

Received 22nd February 2023,
Accepted 30th March 2023

DOI: 10.1039/d3mh00270e

rsc.li/materials-horizons

Narrow response temperature range with excellent reversible shape memory effect for semi-crystalline networks as soft actuators†

Dequan Chi,[a] Haoyu Gu,[a] Jingfeng Wang,[c] Chao Wu,[a] Ruijie Wang,[a] Zhongjun Cheng,[a] Dongjie Zhang,[a] Zhimin Xie[b] and Yuyan Liu *[a]

Complex and controlled reversible actuation inevitably relies on changing thermal fields (direct or indirect) for semi-crystalline reversible shape memory networks. Unfortunately, the non-tunability of thermal signals often brings potential limitations to actuators' applications. In practice, a wide response temperature range (*T*-range) formed by T_{high} and T_{low} in the remarkable reversible actuation is an obvious fact. Herein, we demonstrate the tunability of the transition temperatures while stably maintaining excellent actuation abilities. We further verified that the narrow *T*-range (24 °C) that had not been reported could present more than 17% reversible strain. Special parameter optimization provides opportunities for potential non-implantable biomedical applications. Therefore, based on target 2W-SMP, a vehicle concept with the drug release and vehicle recovery ability was proposed, proving our approach's feasibility.

New concepts

Currently, thermal signals are still considered the main trigger-control mode to present the gratifying trigger-controlled reversible actuations of semicrystalline shape memory polymers. However, extra thermal stimulations are always immutable based on the selected actuation phase. Here, we find an actuation domain with tunability at the level of crystallization thermodynamics based on random copolymerization of two meaningful segments resulting in the formation of a narrow response temperature range. Moreover, this tunable domain allows access to physiological features of the body, while maintaining excellent reversible actuation. The advantages can be verified by applications in the biomedical field, such as drug-coated balloon (DCB) technology. The versatility of our approach allows an extension to other polymer segments that are similar to the structure we have selected.

Introduction

Shape memory polymers (SMPs) have received intense interest due to their ability to realize intelligent shape changes that respond to changes in external stimuli.[1–3] In particular, two-way SMPs (2W-SMPs) can be programmed by one time to transform repetitively between two different shapes.[4–6] These reversible movements under stress-free conditions provide more opportunities to fabricate intelligence units,[7–14] such as soft actuators,[8,9] walking robots[10,11] and artificial muscles.[12–14]

Most 2W-SMPs are typically polymer networks (chemical cross-linking) consisting of actuation and skeleton domains.[15,16] The actuation domains provide a sufficient driving force to achieve reversibly shape-changing switches,[15,17] while the skeleton domains are responsible for maintaining the shape-changing geometry of the 2W-SMPs during the shape-switching process.[15,17,18] In most cases, the liquid-crystalline phase or the crystalline polymer takes the role of actuation domain.[17,19,20] Traditionally, semicrystalline polymer networks are still typical structural models for 2W-SMPs because of their flexible synthesis methods[15,21] and multiple choices in molecular components.[22] Thus, the two-way shape memory effect (2W-SME) arises primarily from the thermal crystal transitions (crystallization and melting) of the actuation domains,[17] which are also referred to as crystal-induced elongation (CIE) and melt-induced contraction (MIC).[6]

Although various types of 2W-SMPs have been reported in recent years,[23] a very important prerequisite for revealing their potential application values is to identify their response conditions and actuation capacity.[24] Thermomechanical tests are helpful in visualizing 2W-SME;[17] that is, some critical parameters of the 2W-SME can be quantified by studying the individual elongation of the network during the heating–cooling cycle, such as the actuation temperature and reversible strain ($\Delta\varepsilon_{rev}$, uniaxial).[25] These parameters are usually expected to have flexible tunability for meeting the background of potential

[a] MIIT Key Laboratory of Critical Materials Technology for New Energy Conversion and Storage, School of Chemistry and Chemical Engineering, Harbin Institute of Technology, Harbin 150001, P. R. China. E-mail: liuyy@hit.edu.cn
[b] National Key Laboratory of Science and Technology on Advanced Composites in Special Environments, Harbin Institute of Technology, Harbin 150080, P. R. China
[c] Northwest Institute for Nonferrous Metal Research, Xi'an 710016, China

† Electronic supplementary information (ESI) available. See DOI: https://doi.org/10.1039/d3mh00270e

applications.[15] For example, an actuating high temperature (T_{high}) close to body temperature should be positive in biomedical fields,[26] a comfortable actuating low temperature (T_{low}) would reduce the dependence on cooling equipment,[27] and excellent actuation is apparently beneficial to complex and flexible macroscopic movements.[28]

In reality, however, it is inconvenient to tune them because these parameters are inherently tied to the crystallization characteristics (thermodynamic and kinetics) of the actuation domains.[22,29] Thus, nearly all semicrystalline networks exhibit the following features in 2W-SME. First, the T_{high} achieved is routinely described as a constant determined by the melting temperature (T_m) of the actuation domains.[15,25] Typical 2W-SM networks containing poly(ε-caprolactone) (PCL) and poly(ω-pentadecalactone) (PPDL), for example, have a seemingly constant T_{high} of 50 °C regardless of the molar ratio of PCL and PPDL.[18,30] In addition, the networks with a broad crystal transition (*e.g.*, crosslinked PCL) also have the most rational T_{high}.[25,31–33] Indeed, recent studies[18,25–34] have shown that T_{high} is generally distributed in the range of 37–90 °C because only limited crystal segments have been developed as an actuation domain. The crystal segments are typically polyester,[25,34] polyether,[26,33] or polyolefin.[32,34] Second, the actuating T_{low} below the cold crystallization transition point (T_{cc}) of the 2W-SMPs is invariably employed, resulting in the recovery of the shape. It is the most widely applied method to ensure that the 2W-SME is completely enforced.[15,17] It seems that the actuating T_{low} of most multiblock copolymer networks is below 0 °C and can even reach −20 °C; for instance, the 2W-SMP, which contained segments of poly(ethylene glycol) (PEG),[35] polytetrahydrofuran (PTHF),[26] and PCL[30,34] associated with its actuation units, showed −10 °C, −15 °C, and −20 °C, respectively. In addition, the crosslinked polyolefin or homopolymer networks always have T_{low} values above 0 °C,[25,31,32] which is generally distributed in the range of 0–25 °C; for example, crosslinked PCL[31] and poly(octylene adipate) (POA)[25] showed the T_{low} values of 10 °C and 5 °C, respectively, while crosslinked poly(ethylene-*co*-vinyl acetate) (EVA)[32] showed a T_{low} value of 25 °C. In practice, previous studies[26,33–35] prefer to use 0 °C as an alternative T_{low} for 2W-SMPs with T_{low} below 0 °C. Third, almost all networks presented $\Delta\varepsilon_{rev}$ (uniaxial) in the 5–25% range under stress-free conditions.[25,28,36] Notably, the actuation strain achieved is generally less obvious in crosslinked PCL and POA, and it is always in the range of 5–7%.[25,37] Moreover, some strategies have been verified to effectively improve reversible actuation, such as building a skeleton of crystallized geometry[16,18] and self-nucleated crystallization.[31]

Theoretically, the key values T_{high}, T_{low}, and $\Delta\varepsilon_{rev}$ are not independent and random but interrelated.[17] As a result, the current state of these parameters has brought an inescapable fact: a wide response temperature range (*T*-range) is always formed by T_{high} and T_{low} when reversible actuation is performed. In detail, statistical analysis[18,25–37] indicates that there is almost 33–70 °C of *T*-range to complete 2W-SME cycles for the semicrystalline networks. The $\Delta\varepsilon_{rev}$ also varies between different *T*-ranges, and there are seemingly unwritten rules between them. The excellent $\Delta\varepsilon_{rev}$ is always accompanied by a wide *T*-range formed by a lower T_{high} and a lower T_{low}, or a higher T_{high} and a lower T_{low}, such as the designated PTHF-*b*-PEG network (T_{high}: 37 °C; T_{low}: −15 °C; $\Delta\varepsilon_{rev}$: 19.5%),[26] as well as the PCL-*b*-PDL networks (T_{high}: 50 °C; T_{low}: −20 °C; $\Delta\varepsilon_{rev}$: 18.5%).[30] Then, a less obvious $\Delta\varepsilon_{rev}$ tended to randomly come out whether in a wide *T*-range or a less-wide *T*-range, similar to the crosslinked PCL–PEG networks[35] (T_{high}: 43 °C; T_{low}: −15 °C; $\Delta\varepsilon_{rev}$: 5%), the crosslinked EVA network[32] (T_{high}: 75 °C; T_{low}: 25 °C; $\Delta\varepsilon_{rev}$: 9%), as well as the crosslinked POA[25] (T_{high}: 38 °C; T_{low}: 5 °C; $\Delta\varepsilon_{rev}$: 7%). The current situation appears to be of little consequence if 2W-SMPs are entirely divorced from the background of potential applications.

We believe, however, that both a wide *T*-range and a less obvious $\Delta\varepsilon_{rev}$ will magnify potential drawbacks and even perturbations if the 2W-SMP performs some complex logic operations as an actuator, such as a medical body micropipe robot.[38] Negative aspects include potential difficulties in generating the temperature field in real-time,[26] possible structural damage[15] (*e.g.*, tissue damage), and poor responses in action.[33] Therefore, narrowing *T*-range innovation by tailoring T_{high} and T_{low} is necessary. In addition, efficient tailoring strategies should be run to obtain/maintain the gratifying 2W-SME rather than heavily sacrificing the benefits of reversible actuation only to meet the requirements mentioned above. However, it seems to present us with a puzzle in designing strategies for 2W-SMPs which is how to achieve a narrow *T*-range and perfect actuation capability in the meantime.

Herein, we report a molecular strategy based on constructing an actuation domain with tunability at the level of crystallization thermodynamics to achieve the above. This unique tunability was attributed to the high (crystalline) compatibility between the PCL and POA segments, resulting in cocrystalline (isodimorphic) structures.[39] That is, a broad crystal transition could be tuned by preparing typical 2W-SM networks composed of POA and PCL with different mass fractions, but did not significantly decrease the crystallinity of the networks.[40] In contrast, reduction of the crystalline phase is often detrimental for 2W-SME.[41] Thus, the strategy effectively ensured the tailoring of T_{high} and T_{low} without significantly weakening the reversible actuation for POA-*b*-PCL crosslinked networks. This resulted in the presentation of a rewarding actuation strain (17.6%) in only the 24 °C of *T*-range formed by 43 °C (T_{high}) and 19 °C (T_{low}). Optimization results were then positive for biomedical fields.[38] In the case of our material, suitable actuation temperatures would minimize potential tissue damage,[42] the narrow *T*-range might also reduce the difficulties of performing thermal cycling as much as possible,[21] and the excellent actuation provided more possibilities for 2W-SMP's complex shape switching. For this reason, we designed a vehicle model using our material as a potential non-implantable biomedical application. Specifically, the specified material with a pre-programmed double helix structure could simulate the drug release and vehicle recovery process in a vascular model. This inspiration had been taken from drug-coated balloon technology (DCB),[43] in which the introduction and export of gasses

lead to a balloon with reversible expansion and contraction, thereby completing the release of the drug. This is the first report on the easy tuning of the *T*-range of 2W-SME to meet more practical applications for 2W-SMPs.

Materials and methods

Materials

Adipic acid, 1,8-octanediol, scandium triflate, 2-isocyanate ethyl methacrylate, and dibutyltin dilaurate were purchased from Aladdin Reagent Co., Ltd. Pentaerythritol tetrakis(3-mercapto propionate) (PTMP) and 2,2-dimethoxy-2-phenyl acetophenone (DMPA) were purchased from Shanghai Macklin Biochemical Co., Ltd. Petroleum ether and dichloromethane were purchased from Sinopharm Chemical Reagent Co., Ltd. In particular, PCL-diol with a number average molecular weight (M_n) of 10 000 g mol^{-1} and polydispersity index (PDI) of 1.7 (Fig. S5, ESI†) was provided by Daicel (China) Investment Co., Ltd. All chemicals were used as received without further purification.

Synthesis of chemical intermediates

The methods for preparing all chemical intermediates POA-diol, POA-dimethacrylate (POA-DA), and PCL-dimethacrylate (PCL-DA) used in this study can be found in Schemes S1–S3, ESI.† The molecular structure details of all intermediates were confirmed to be correct by ^{1}H NMR (Fig. S1–S4, ESI†). Moreover, the synthesized POA-diol had an M_n of approximately 7000 g mol^{-1} and PDI of 2.3 (Fig. S5, ESI†).

2W-SMP synthesis

Taking the example of a 2W-SMP composed of POA and PCL with a weight ratio of 3/7 between them, both POA-DA (1.5 g, 0.21×10^{-3} mol) and PCL-DA (3.5 g, 0.35×10^{-3} mol) were fully dissolved in 10 mL of dichloromethane. Then, PTMP (0.137 g, 0.28×10^{-3} mol) as a chemical crosslinker and DMPA (6.5×10^{-3} g) as a photoinitiator were added to the oligomer solution and stirred for several minutes. The precursor solution was poured into a quartz boat mold (8 cm (length) × 4 cm (width) × 1 cm (height)). The mixture was irradiated under ultraviolet light for 5 min (intensity: 100 mW cm^{-2}). The obtained film was dried under vacuum for 24 h. Other 2W-SMPs with various weight ratios were synthesized following the same procedure.

Characterization of 2W-SME

The key values T_{high}, T_{low}, and $\Delta\varepsilon_{rev}$ were measured using a TA-Q850 DMA working in the controlled force mold for all synthesized 2W-SMPs. Detailed operations can be described as follows: a selected sample with dimensions of 20 mm (length) × 5 mm (width) × 0.5 mm (thickness) was first heated to 63 °C under a zero-stress mode to erase the thermal history. Then, constant stress was applied, and the temperature was reduced from 63 °C to −10 °C at 3 °C min^{-1}. Afterward, the stress was unloaded, and the sample was heated to T_{high} and cooled to T_{low} at a rate of 3 °C min^{-1} reversibly to obtain multiple reversible shape memory curves. The strains at T_{low} and T_{high} were denoted ε_{act} and ε_{low}, respectively. The reversible $\Delta\varepsilon_{rev}$ was evaluated by $\Delta\varepsilon_{rev} = \varepsilon_{act} - \varepsilon_{low}$.

Microanalysis

Small-angle X-ray scattering (SAXS) and wide-angle X-ray scattering (WAXS) were performed using a Xenocs X-ray small-angle scatterometer (Xeuss 2.0, France) for the selected sample (including both stretched and unstretched states). Sample-to-detector distance calibration and beam center were performed using dry rat tail tendons. Moreover, the microstructural evolution of the selected sample (stretched state) during the heating–cooling cycles was also explored by *in situ* SAXS and WAXS. The heating and cooling rates were both 5 °C min^{-1} to collect scattering patterns. Both SAXS and WAXS patterns of the stretched sample were collected at 14 °C and 43 °C with two cycles, and they could be transformed into 1D profiles by integration with Fit2D software. The peak q_{max} (1D-SAXS profiles) is related to the long period (L) by Bragg's law: $L = 2\pi/q_{max}$, where q is the scattering vector.

Methods involving sample pretreatment, including the stretched sample and the sample for demonstration, have been provided in the ESI.†

In addition, details about other characterizations related to 2W-SMPs, or chemical intermediates are also listed in the ESI,† including thermal analysis (DSC), gel content analysis, Fourier infrared (FTIR), X-ray diffraction (XRD), cytotoxicity assay, water absorption test, gel permeation chromatography (GPC), and ^{1}H NMR.

Results and discussion

The target 2W-SMPs were successfully synthesized by thiol-ene click chemistry of POA-DA, PCL-DA, and PTMP under UV-irradiated conditions (Scheme S4, ESI†). Specifically, free-radical reactions (photo polymerization) can occur through these thiol groups of PTMP and –C═C– bonds of PCL-DA or POA-DA in the presence of the photoinitiator DMPA.[34] Thus, PTMP is a cross-linking point to connect the POA or PCL chain segments at will, resulting in the formation of a crosslinked copolymer network (Fig. 1(a)). Then, the synthesized 2W-SMPs were denoted C-POA$_x$PCL$_y$, where x/y (varies from 1/9 to 9/1) is the ratio of the weight percentage between POA-DA and PCL-DA. Comparing the FT-IR spectra of the intermediates and all C-POA$_x$PCL$_y$ networks (Fig. S6 and S7, ESI†), the latter showed that the absorption intensity of the ═CH at 811 cm^{-1} had disappeared almost completely. This indicated that the thiol groups and –C═C– bonds in all networks were almost fully linked by exposure to ultraviolet radiation.[10,26] Moreover, all samples (including crosslinked POA (C-POA) and crosslinked PCL (C-PCL)) were subjected to the equilibrium swelling test to obtain their degree of cross-linking. Their swelling degree and gel content in toluene were approximately the same, distributed between 2.88–3.30 and 96.4–98.7%, respectively (Fig. S8, ESI†). This ensured that all networks' anisotropy and spatial

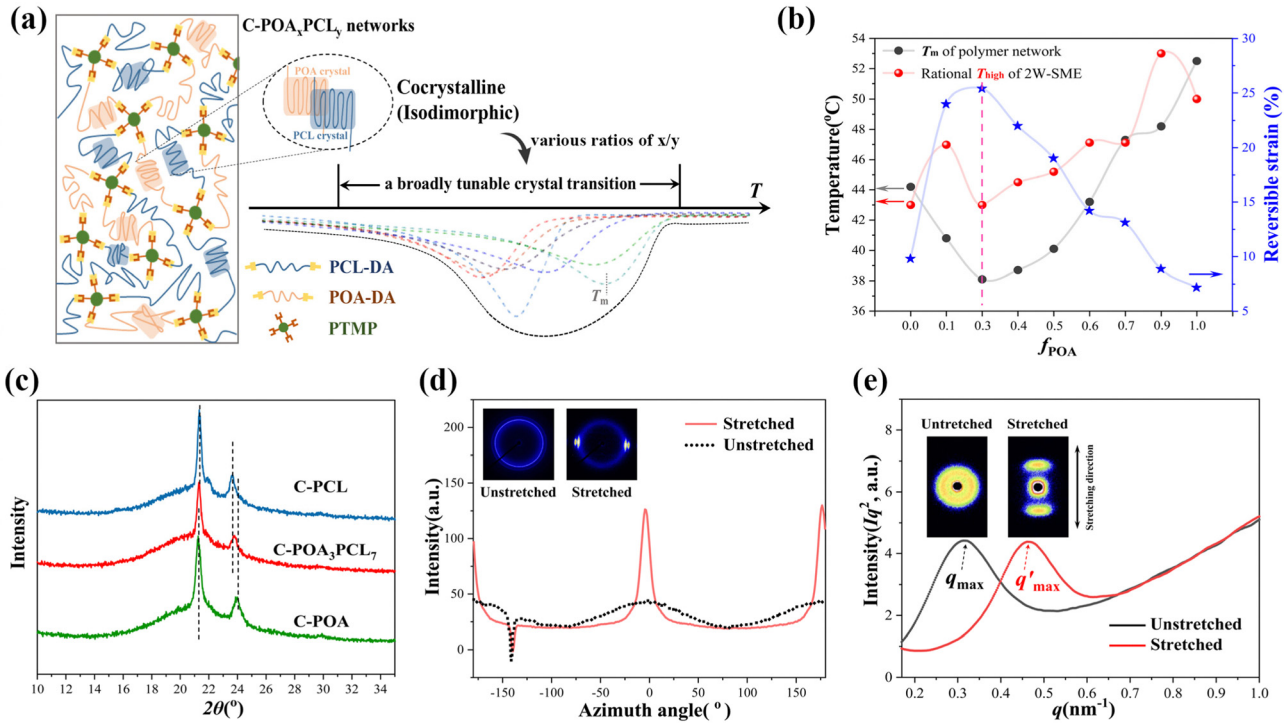

Fig. 1 Microstructure and 2W-SME of C-POA$_x$PCL$_y$ networks. (a) The mechanism for constructing a broadly tunable crystal (melting) transition in the 2W-SMP networks. The various colored curves (dotted lines) on the right represent the heating curves (DSC analysis) of the networks with different components. This means that the crystal (melting) transition range of the C-POA$_x$PCL$_y$ networks would be distributed within the crystal (melting) transition range shown by the black dotted line. (b) The relationship between T_{high} and T_m with the change in f_{POA}, and the evaluation of 2W-SME at their respective rational T_{high} under stress-free conditions. All polymer networks were selected at 4 °C as the T_{low} in the 2W-SME test. Rational T_{high} means that there is the largest reversible strain ($\Delta\varepsilon_{rev}$) in the temperature of T_{high}. f_{POA} means the weight percentage of POA segments relative to the total macromonomer amount. (c) XRD patterns of the C-POA, C-PCL and C-POA$_3$PCL$_7$ networks. They exhibit major characteristic crystalline peaks at 2θ of *ca.* 21.2–21.3° and 23.6–23.9°. (d) Azimuthal scattering curves of 2D WAXS patterns of unstretched (left) and stretched (right) C-POA$_3$PCL$_7$ networks in the insert map obtained by 360° integrations. The stretched C-POA$_3$PCL$_7$ crystallized under a load of 0.8 MPa. (e) SAXS intensity Iq^2 *vs.* scattering vector q obtained for unstretched slowly crystallized and stretched crystallized samples of C-POA$_3$PCL$_7$. The stretched sample was treated as above (d). (e) SAXS intensity Iq^2 *vs.* scattering vector q obtained for unstretched slowly crystallized and stretched crystallized C-POA$_3$PCL$_7$. The stretched sample was treated as described above (d).

distribution tended to be the same.[44] Meanwhile, the very low water absorption distribution of 0.4% to 0.6% for all samples indicated that humidity or water does not affect the 2W-SME of the samples (Fig. S9, ESI†).

Fig. 1(a) shows the principle of the broadly tunable crystal (melting) transition for target 2W-SMPs. The idea for this principle grew out of the thermal behaviors of isodimorphic random copolyesters, whose cocrystallinity (isodimorphism) is manifested by the system always maintaining a high crystallinity and a decrease in the T_m of the crystalline phase as the comonomer content increases until a minimum value is reached.[45] This also applies to copolymer networks consisting of POA and PCL due to their similar crystallographic characteristics.[46] We first illustrated the isodimorphism mechanism in the cocrystalline system of networks *via* DSC and XRD. On the one hand, a single-phase transition process (Fig. S12 and S13, ESI†) was observed in all copolymer networks during the heating and cooling scans, although they contained both the POA and PCL phases. That is, the excellent crystal compatibility of the POA and PCL phases allowed the C-POA$_x$PCL$_y$ to maintain a wide melting transition, regardless of the ratio of x and y.

On the other hand, the crystallizability of all C-POA$_x$PCL$_y$ networks was not greatly depressed or even sharply destroyed when the comonomer unit POA was introduced compared to C-PCL, and the crystallinity of the networks ranged from 18.2 to 30.1% (Table S1, ESI†). This is favorable for the 2W-SME, minimizing the possibility of a weak actuation ability due to a reduction in the crystallizability of the network.[15,47] In addition, the compatibility of the two phases was also reflected visually in the crystal structure (Fig. 1(c)). Insignificant differences in diffraction peaks between C-POA$_3$PCL$_7$ and C-POA/PCL proved that the interaction of the two phases did not produce a new crystal structure. Similar results can be found in other products (Fig. S10, ESI†). More importantly, the T_m of the C-POA$_x$PCL$_y$ networks also tended to decrease and then increase as the content of introduced POA segments increased (Fig. 1(b)), similar to the thermal behaviors of cocrystallinity (isodimorphism). Therefore, a broad crystal (melting) transition could be tuned in the range of 30–55 °C by changing the weight ratio of POA and PCL segments (Fig. S12, ESI†), and T_m is also tunable in the range of 38–48 °C (Table S1, ESI†). Notably, the C-POA$_3$PCL$_7$ network showed the lowest T_m (38 °C), indicating that it had pseudoeutectic structures.[45]

The positive correlation between T_{high} and T_m would result in T_{high} being tunable based on a general mechanism of reversible shape memory in semicrystalline elastomers.[25] The 2W-SME of all prepared networks was explored by DMA analysis under stress-free conditions. Although a broad melting transition in a semicrystalline network allows for multiple choices of T_{high} with different degrees of reversible actuation, a rational T_{high} should often match an optimal reversible actuation. Accordingly, Fig. 1(b) also shows the evolution trend of the rational T_{high} with different C-POA$_x$PCL$_y$ networks, similar to the variation in T_m. Furthermore, the rational T_{high} of these samples was always higher than the T_m of the sample to which they correspond, contrary to what has been previously reported.[33] This phenomenon comes from the preprogramming mechanism of the samples. Taking sample C-POA$_3$PCL$_7$ as an example, the stretched sample showed a higher melting transition than the original (Fig. S14, ESI†), which indicated that crystals with higher melting points were easily produced under conditions of applied stress. Therefore, it was necessary to study the crystalline state of the samples in the programmed state.

WAXS and SAXS analyses were recorded to determine the difference in the crystals between C-POA$_3$PCL$_7$ in its original state (slow crystalline formation) and the stretched-oriented state (Fig. 1(d) and (e)). Compared with the original sample, the 2D-WAXS pattern of the stretched sample showed a scattering concentration in the equatorial direction, reflecting the preferred orientation of the crystals. The curve of the azimuthal angle originating from the 2D-WAXS pattern (stretched sample) allowed the symmetry of the oriented crystals to be determined, which, unlike the classical orthorhombic in the symmetry of PCL oriented crystals, tended to display more of a monoclinic crystal system, as reported by POA.[46,48] We believe that POA crystals rather than PCL crystals strand along the stretched pathway to create the architectural scaffold of the temporary shape. Thermodynamically, the amorphous POA segments crystallize ahead of the PCL segments along the stress direction during the physical programming stage, based on the difference between the two phases arising during cold crystallization (Fig. S11, ESI†). In addition, the long period (L) of the stretched sample was smaller than that of the unstretched sample, and they were 13.5 nm and 20.3 nm, respectively, as calculated directly by Bragg's law (Fig. 1(e)). In other words, the lamellae of the regenerated crystals were thinned during the reprogramming mechanism, rather than the network showing increased crystallinity as reported previously.[34] This could be explained by the fact that the POA and PCL lamellae in the original network initially overlapped each other to form a single large lamella because of their similar periodicities.[49] In contrast, the preferentially formed (POA) lamellae in the stretched network could not be stacked with the later lamellae due to the sequential order of crystallization.

It was also important to evaluate the reversible actuation for each network at its corresponding rational T_{high}. The $\Delta\varepsilon_{rev}$ between the rational T_{high} corresponding to each network and the constant T_{low} of 5 °C showed a tendency to increase and then decrease with the increase in POA units in the C-POA$_x$PCL$_y$ networks (Fig. 1(b)). The $\Delta\varepsilon_{rev}$ reached the maximum for C-POA$_3$PCL$_7$, which was more than 25%. Correspondingly, the samples of C-POA$_1$PCL$_9$ and C-POA$_4$PCL$_6$ also had more than 20% $\Delta\varepsilon_{rev}$. However, C-POA$_3$PCL$_7$ had the lowest T_{high} compared to the other networks. Therefore, reducing T_{high} (or achieving tunable T_{high}) by constructing isodimorphism structures in multiphase semicrystalline 2W-SMPs would be feasible.

More interestingly, this unique isodimorphic mechanism could also show another advantage. For a given network, its remarkable reversible actuation allows T_{high} to be distributed over a range of temperatures rather than a constant value. In Fig. 2(a), more than 20% of $\Delta\varepsilon_{rev}$ could be stimulated in the range of 41–47 °C at T_{high}. A similar result was also found in the C-POA$_4$PCL$_6$ network (Fig. S15, ESI†). In addition, other networks, such as C-POA$_1$PCL$_9$ and C-POA$_5$PCL$_5$, showed more than 15% of $\Delta\varepsilon_{rev}$ in the range of 43–47 °C at T_{high}, as shown in Fig. S16 and S17, ESI.† This result indicated that these networks would have multiple choices in T_{high} without heavily losing reversible actuation. We thought the multiple-choice model in T_{high} would best serve the needs of application diversity.[17] Meanwhile, further studies, such as reversible bending experiments in Fig. 2(b), were conducted to visually understand this superiority. Different amplitudes of actuation were obtained in temperature cycles with different T_{high}s (40–47 °C) and constant T_{low} (5 °C) by introducing a preprogrammed folding shape for C-POA$_3$PCL$_7$. It was noteworthy that the sample would sacrifice the original temporary shape rather than reduce the change in the actuation angle (the angle difference at various T_{high}s and a fixed T_{low}) when the T_{high} was further increased. It is an infrequent observation that the actuation angle has been on the rise because the actuation degree usually decreases with increasing T_{high} for other 2W-SMPs that have been developed.[26,31] The network had a maximum actuation angle of approximately 120°, but its shape was approximately 30° different from the original temporary shape, which was the result of a higher T_{high} destroying a part of the shape memory skeleton phase.

Tunable T_{high}s within the various networks and multiple choices of T_{high}s in the single network alone did not satisfy the requirements of designing a narrow T-range. Therefore, tailoring T_{low} was also necessary without seriously weakening the actuation capability of the networks. As shown in Fig. 2(c), C-POA$_3$PCL$_7$ underwent reversible strain switching under temperature cycles between a constant T_{high} (43 °C) and various T_{low}s (0–24 °C). As expected, since the recovery of actuation usually relied on the nonisothermal crystallization kinetics of the actuation domains,[17] T_{low} at 4–19 °C showed a slight decrease in $\Delta\varepsilon_{rev}$ (compared to the 21% of $\Delta\varepsilon_{rev}$ at T_{low} of 0 °C, Fig. 2(c)), which indicated that although C-POA$_3$PCL$_7$ had a single T_{cc} of 6.7 °C (Fig. S13, ESI†), the cold crystallization of the network could be triggered at 4–19 °C. The $\Delta\varepsilon_{rev}$ values at T_{low} values of 4 °C, 9 °C, 14 °C and 19 °C were 19.4%, 18.7%, 17.9% and 16.3%, respectively. This is true not just with the above but with other networks; for example, C-POA$_1$PCL$_9$, C-POA$_4$PCL$_6$, and C-POA$_5$PCL$_5$ in Fig. S18 and S20, ESI,† showed $\Delta\varepsilon_{rev}$ values

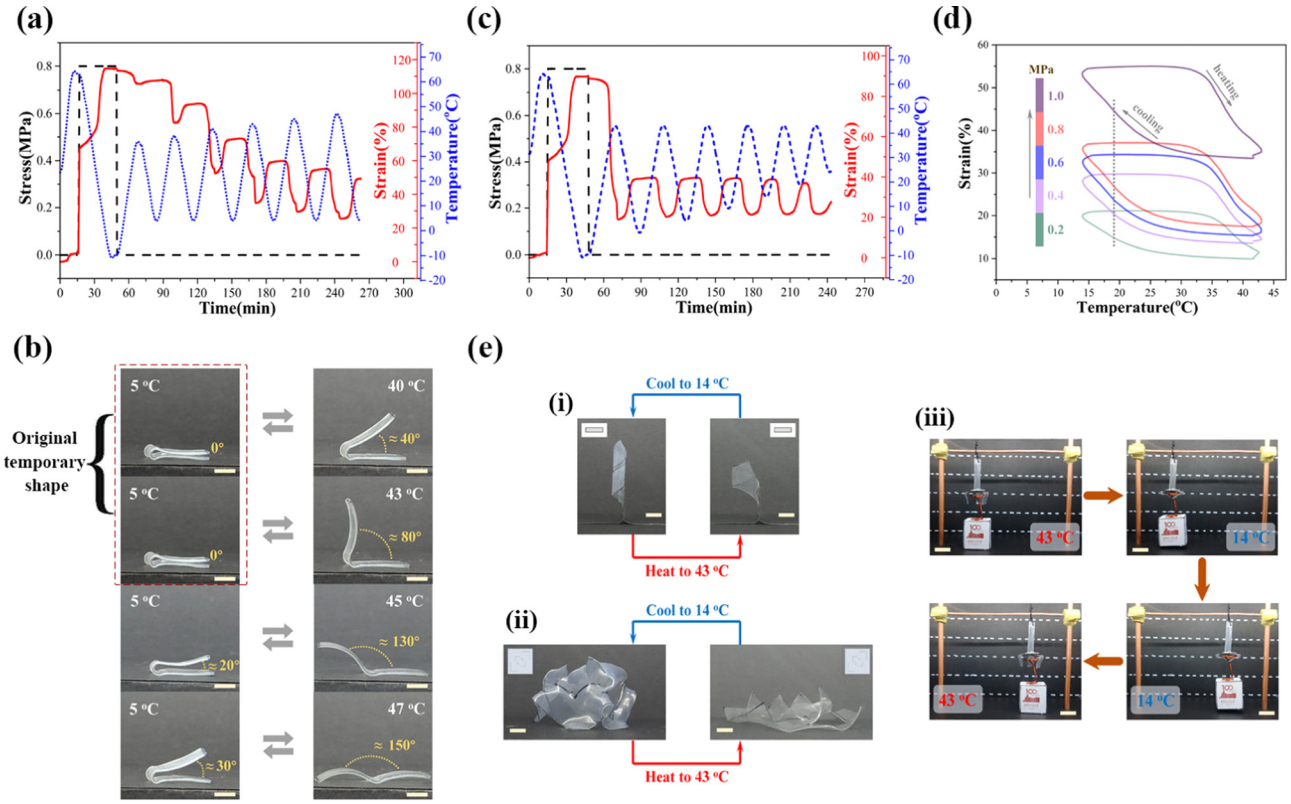

Fig. 2 The evaluation and presentation of 2W-SME for the C-POA$_3$PCL$_7$ network. (a) Reversible shape memory cycle between a variable T_{high} and a fixed T_{low} of 4 °C. The corresponding T_{high} values were 36 °C, 38 °C, 41 °C, 43 °C, 45 °C, and 47 °C, respectively. (b) Reversible bending experiments conducted between different T_{high} values and a fixed T_{low} of 5 °C under stress-free conditions. The T_{high} and T_{low} values were obtained by measuring the real-time temperature of the environment where the sample was located through the temperature sensor. Scale bar: 5 mm. (c) Reversible shape memory cycle between a variable T_{low} and a fixed T_{high} of 43 °C. The corresponding T_{low} values were 0 °C, 4 °C, 9 °C, 14 °C, 19 °C and 24 °C, respectively. (d) The 2W-SME curves of the second cooling/heating cycles represented as the absolute strain change *vs.* temperature curves for the various applied initial tensile stresses. The dotted line indicates the actuation strain increment. (e) Complex shape deformations and shape memory devices fabricated from the C-POA$_3$PCL$_7$ network. For example, (i) shape change between closing and unfolding of the 3D-tubular curl of sample. The inset images illustrate the original shape from the top view. Scale bar: 5 mm. (ii) Cooperative shape change of the 3D-support structure in space *via* paper-cutting art. The inset images illustrated the paper-cut patterns from the top view. Scale bar: 8 mm. (iii) A soft gripper was designed through customized paper-cutting art. The gripper was closed and opened during cooling–heating cycles, and was used to move a small box with a handle. Scale bar: 10 mm.

distributed in 15.3%–18.7%, 15.8%–19.8%, and 14.1–16.4% at T_{low} values of 4 °C, 9 °C, 14 °C and 19 °C, respectively. However, $\Delta\varepsilon_{rev}$ at a T_{low} of 24 °C yielded more than half loss compared to $\Delta\varepsilon_{rev}$ at a T_{low} of 0 °C for C-POA$_1$PCL$_9$, C-POA$_3$PCL$_7$, C-POA$_4$PCL$_6$, and C-POA$_5$PCL$_5$, resulting in greatly reduced actuation capability. In other words, 24 °C only limitedly triggered cold crystallization in the actuation domain. Therefore, the T_{low} of the above networks could be randomly tailored from 0–19 °C.

Additionally, different values of axial tensile stress, which were applied to networks in the physical programming stage, showed huge effects on actuation capability, as in previous reports.[34,50] Taking C-POA$_3$PCL$_7$ as an example, $\Delta\varepsilon_{rev}$ rose to 21% from 10% when the applied tensile stress was loaded in the range from 0.2 to 1.0 MPa (Fig. 2(d)). That is, the change in $\Delta\varepsilon_{rev}$ was positively related to increased stress, and this relationship gradually weakened until the actuation capability was constant. So, a preprogrammed stress of 0.8 MPa was used to evaluate the 2W-SME for all C-POA$_x$PCL$_y$ networks at various T_{high} or T_{low} states. Not only that but some details about the actuation mechanism could also be observed during cycles with different stresses. Only one-step strain elongation was observed in the cooling stage, regardless of the change in tensile stress. More importantly, Fig. S22, ESI† originated from the correlation in Fig. 2(c) and showed similar one-step strain elongation at different T_{low} values. That meant only a single phase transformation occurred during the network's CIE process.[34]

Overall, for a single C-POA$_x$PCL$_y$ network, remarkable $\Delta\varepsilon_{rev}$ can respond at the selectable T_{high} and T_{low}, both of which were distributed in a suitable temperature range. For example, for the C-POA$_3$PCL$_7$ network, $\Delta\varepsilon_{rev}$ with a range of 16%–25% would be presented between T_{high} with a range of 41–47 °C and T_{low} with a range of 0–19 °C. We picked a T_{high} of 43 °C and a T_{low} of 14 °C within which actuation occurs as visual presentations. As shown in Fig. 2(e)-(i), the 1D-strip sample was programmed as a 3D-tubular curl shape, and then the shape change between closing and unfolding of the tube structure was realized through the reversible temperature field between 43 °C and

14 °C. The origami-inspired design also enabled the preprogrammed 3D-support structure, such as Fig. 2(e)-(ii), resulting in a cooperative reversible shape switching between 3D space and 1D planes. Moreover, a three-arm manual gripper was designed to complete the grasping and releasing of a small box with a handle. The three claws can be collaboratively opened or closed between 43 °C and 14 °C. The programmability of the complex shape and the collaborative shape change could provide more possibilities for the application of products.

In the literature, there have been previous reports on the microstructure evolution mechanism of the 2W-SME for semicrystalline elastomers.[17,22,26–30] For multiphase systems, the actuation domains seem to favor the phase with a lower melt transition, while the phase with a relatively high melt transition prefers the skeleton domains; for example,[35] in 2W-SMPs composed of PCL and PEG ($T_{m,PCL} > T_{m,PEG}$), PEG crystals act as actuation domains and PCL crystals act as skeleton domains. However, the C-POA$_x$PCL$_y$ networks do not seem to follow the above rules, although the POA phase has a higher melt transition than the PCL phase. So, it is necessary to explore the evolution mechanism of the C-POA$_x$PCL$_y$ networks in the 2W-SME. *In situ* SAXS and WAXS are universal tools for investigating the microstructural evolution of shape memory networks.[18,32,36] These networks include homogeneous and multiphase networks prepared by any cross-linking method.[26,30,34,47]

As shown in Fig. 3(a) and (b), 2D WAXS and SAXS patterns of the typical C-POA$_3$PCL$_7$ network were obtained *via* two cycles between a T_{high} of 43 °C and a T_{low} of 14 °C to confirm the microstructure evolution during its 2W-SME. First, the 2D WAXS and SAXS patterns at 43 °C had a scattering concentration in the equatorial and meridian directions, predicting that even though the temperature was higher than T_m, these oriented crystals did not wholly disappear and acted as the geometric skeletons that maintained the temporary shape at 43 °C. Meanwhile, the WAXS data (Fig. 3(a)) further explained the dynamic mechanism of the crystal parameters. In each shape memory cycle, there were no particular Miller indices because the 1D-WAXS curve was similar to the curve of the original sample (Fig. 1(c)). This result indicated that no new crystal structures were generated during the 2W-SME. The constant change of interplanar spacing (d) and scattering intensity based on the general Bragg's equation ($2d \sin\theta = n\lambda$) during the 2W-SME meant that the lattice constants of the skeleton phase and actuation phase are likely to be the same. More importantly, according to the crystallographic database,[46] the two diffraction peaks located at 2θ = 21.4° and 24.0° were related to the (110) and (200) planes. Besides, 2D SAXS patterns (Fig. 3(b)) at 43 °C and 14 °C verified that the crystalline morphology of the actuation phase exhibited full reversibility of the crystallite dimensions and orientations. The long period (L) at 43 °C and 14 °C was calculated *via* a function of scattering

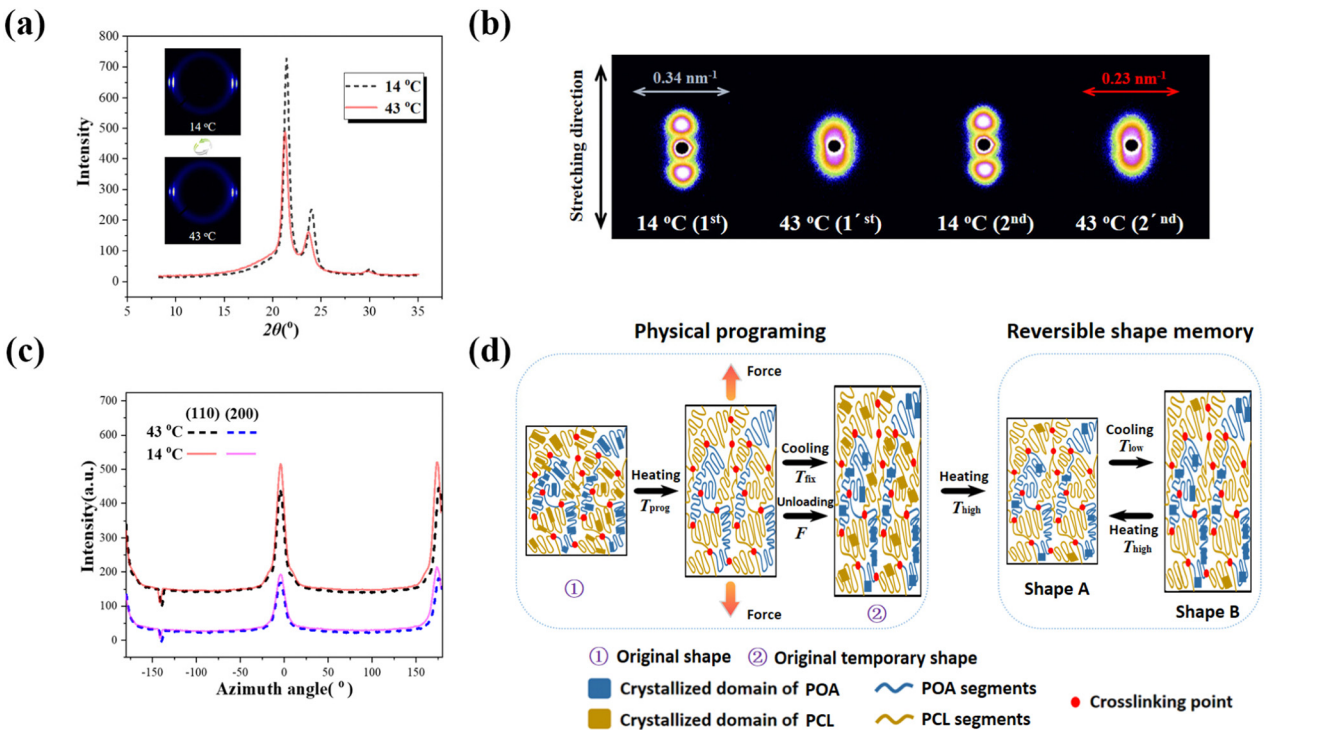

Fig. 3 Evolution mechanisms of microstructures in the reversible shape memory behavior of the C-POA$_3$PCL$_7$ network. (a) *In situ* 2D-WAXS patterns at T_{high} = 43 °C (bottom-left) and T_{low} = 14 °C (top-left), and their corresponding 1D-WAXS scattering curves. (b) Structural changes occurring during the 2W-SME cycle determined by *in situ* 2D-SAXS. (c) Changes in azimuthal scattering curves obtained by 360° integrations over two intervals of angle 2θ at the (110) plane and (200) plane reflection from the above 2D-WAXS patterns of (b). (d) Microstructure evolution model of the 2W-SME under stress-free conditions.

vector q of Fig. S23, ESI,† as 23.7 nm and 18.5 nm, respectively. We suggested that this resulted from the reversible disappearance and generation of tiny lamellae in the network during the temperature cycles.[32]

Then, the intensity *vs.* azimuthal angle curves were obtained by 360° integrations of the WAXS images in Fig. 3(a) over the above two scattering angles 2θ, as shown in Fig. 3(c). The (110) and (200) planes were oriented along the equatorial direction, which was different from what was reported previously.[37] For typical PCL–PDL copolymer networks,[34] the scattering profiles (including the (110) and (200) planes) of the stretched samples are generally oriented along the meridian direction because PCL crystals and PDL crystals are capable of producing cocrystalline (isomorphic) structures, *i.e.*, representing orthorhombic and pseudo-orthorhombic structures, respectively. Therefore, we ruled out the possibility of PCL crystals as the actuation domains in the C-POA$_3$PCL$_7$ network. In addition, we found that the (110) and (200) faces of monoclinic crystals tend to be oriented more along the equatorial direction,[51] while most of the crystals of polyesters are usually monoclinic.[46] Thus, we presumed that POA crystals played the role of driving domains. The full width at half maximum (FWHM) of the (110) plane, as well as the orientation intensity, changed distinctly and reversibly, while the (200) plane did not change significantly between 43 °C and 14 °C. As a result, we suggested that the POA crystals with the (110) plane acted as driving domains, and those with the (200) plane acted as skeleton domains in C-POA$_3$PCL$_7$. This also explained why the T_{low} of C-POA$_3$PCL$_7$ can be distributed in the range of 0–24 °C, while the T_{cc} was 6.7 °C.

Based on the above analyses, a microstructure evolution model was established to visually describe the progress of 2W-SME, citing C-POA$_3$PCL$_7$ as a typical reversible actuation network, as shown in Fig. 3(d). Despite the single cold crystalline domain in cooling scanning (Fig. S13, ESI†), we still believe that the target network has two crystallization processes in the physical programming stage. In detail, the original network (original shape) contained the PCL and POA crystalline domains and was heated to the shape programming temperature (T_{prog}, $T_{prog} > T_m$) to eliminate the thermal history. Then, the network was cooled to the shape fixed temperature (T_{fix}, $T_{fix} < T_{cc}$) under a constant external force (F). In this process, part of the POA segments crystallize first along the axis of F leading to the fabrication of a shape memory skeleton. Next, the free POA and PCL crystalline phases were distributed in the network during further cooling to obtain a stable original temporary shape. Uniquely, the thermodynamic parameters of oriented POA crystals could be tuned based on the content of POA segments in the network.

In the reversible shape memory stage, part of the oriented POA crystals and most of the free PCL crystals were destroyed when the network was heated to T_{high}. Therefore, the shape memory skeleton was no longer stable, resulting in a change in the temporary shape, and the degree of change was affected by T_{high}. Meanwhile, the remaining unmelted POA-oriented crystals act as the skeleton phase maintaining another temporary shape (Shape A) at the T_{high}. We hypothesized that there might be sporadic unmelted free PCL crystalline domains simultaneously. The shape change's essence is that the crosslinking point is no longer constrained by the crystalline domain and is activated, thus releasing the entropy elasticity of the molecular segments. However, most of the oriented POA crystals that had been destroyed at T_{high} would restore their original dimensions and orientations, resulting in the recovery of the temporary shape (Shape B) when the network was cooled to T_{low}. Most notably, the network no longer formed a PCL crystalline domain because T_{low} was higher than the T_{cc} of the PCL segments (Fig. S11, ESI†). This meant that the POA crystals would independently show the thermodynamic characteristics of their molecular chains.

Thus far, an effective tailoring strategy aiming to achieve remarkable reversible actuation in a narrow T-range seems feasible owing to multiple choices in T_{high} and T_{low} for a single C-POA$_x$PCL$_y$ network and tunable T_{high}s within the various C-POA$_x$PCL$_y$ networks. C-POA$_3$PCL$_7$ was chosen as the preferred 2W-SMP because it had the lowest T_m (resulting in the lowest rational T_{high}) as well as the largest $\Delta\varepsilon_{rev}$. Then, the reversible strain-switching experiments were performed during multiple heating–cooling cycles between T_{low}s of 14 °C and 19 °C and a fixed T_{high} of 43 °C to verify the above purpose. Nicely, stable, and excellent $\Delta\varepsilon_{rev}$ was revealed, that is, around 19% in the T-range of 29 °C and 17% in the T-range of 24 °C, respectively, as shown in Fig. S21, ESI,† and Fig. 4(b).

It was a positive optimization that produced extremely useful results. C-POA$_3$PCL$_7$ offered the possibility of 2W-SMPs being used as potential non-permanently implanted biomedical actuators. First, its suitable actuation temperatures (including T_{high} and T_{low}) minimized potential tissue damage. This was because, according to the current literature, irreversible cell thermal damage occurred only under long thermal conditions (30–60 min) when the temperature was 40–45 °C, and the thermal action time to achieve irreversible damage decreased exponentially when the temperature was higher than 60 °C.[52] Generally, the time required for shape changes of thermally-induced 2W-SMPs depends on the heated medium and whether the heat source is in direct contact with the matrix. Several studies[25,34] have also proved that the shape-switching time was always less than a minute under direct contact with the heat source. For the C-POA$_3$PCL$_7$ network, it only takes a few minutes to go from 37 °C to 43 °C (if the heating rate is 1 °C min^{-1}), and the thermal stimulation time is very short at 43 °C. Furthermore, some researchers have carefully claimed that ice crystals slowly form in the extracellular fluid when the cellular components approach the ambient temperature to 0 °C.[53] Consequently, a T_{high} of 43 °C and a T_{low} of 19 °C were safe temperatures for the human body. By the way, SMPs as potential implants or semi-permanent implants prefer to have their T_{high} at 36–37 °C, which is positive because they can rely on body temperature to achieve self-actuation.[54–56] But, it is not necessary for 2W-SMPs as non-implanted biomedical actuators to tune the T_{high} to 36–37 °C, only to the safe temperature range of the human body, since the actuators sometimes need to avoid being actuated by body temperature.

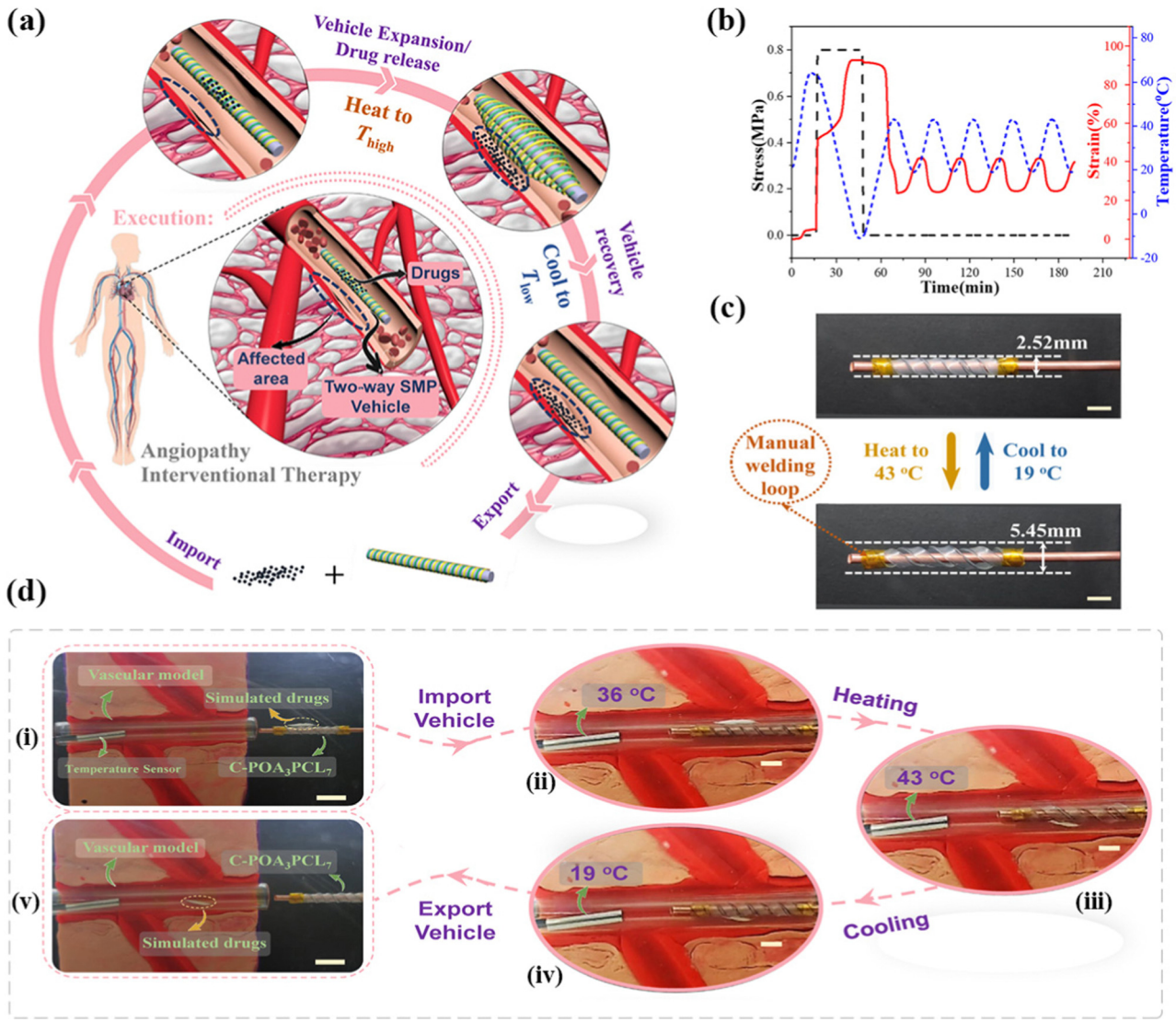

Fig. 4 Biomedical application of the polymer network as a drug delivery vehicle in blood vessels. (a) Graphic illustration of the process of drug release and vehicle recovery based on the 2W-SMP double-helix structure. The color of the spiral structure is only used to identify it as a double-helix rather than a single-helix, and has no other special meaning. (b) Stable and gratifying 2W-SME cycles of the C-POA_3PCL_7 network between T_{high} = 43 °C and T_{low} = 19 °C. (c) Demo example of the reversible diameter change of the double-helix structure in 2W-SME. The double-helix structure was made *via* two C-POA_3PCL_7 strips with the same length and width. Scale bar: 5 mm. (d) Photos showing the rotating expansion and contraction process of the double-helix structure to complete the drug release and vehicle recovery progress based on the 2W-SME of the C-POA_3PCL_7 network. The temperature sensor is used to prove that our design is based on direct heating and cooling of the double-helix structure, rather than simple heating of the human body or local tissue. Scale bar: 12 mm (i and v), 5 mm (ii, iii and iv).

Second, a narrow T-range of 24 °C between a T_{high} of 43 °C and a T_{low} of 19 °C reduced the difficulty of creating a cyclic temperature field.[21] For example, medical robots prepared by C-POA_3PCL_7 could accomplish potential medical applications by directly spraying saline that was 43 °C and 19 °C, respectively. To ensure the continuity of the demonstration experiment, we used air heating and cooling in Fig. 4(d), but this does not mean that the above method was not feasible. The biotoxicity experiment of C-POA_3PCL_7 was performed, as shown in Fig. S27, ESI,† and the results showed that the sample was weakly biotoxic and caused less potential damage to tissue cells. More importantly, the $\Delta\varepsilon_{rev}$ of 17% with only 24 °C of response temperature range allowed for the design of complex and reversible shape switching.

Therefore, combined with commercial drug-coated balloon (DCB) technology,[43] we designed a vehicle with drug release and vehicle recovery using C-POA_3PCL_7, as shown in Fig. 4(a). Specifically, DCB technology uses the balloon catheter as a tool to deliver drugs to the site of the vascular lesion, and then the drugs are completely released in a short time when the balloon contacts the vascular wall through expansion to avoid continuous stimulation of the implanted drug carrier. In this technology, the reversible behavior of the balloon between expansion and contraction is a crucial player. Nevertheless, it

usually requires complex pneumatic equipment and special expansion skills of the operator to control carefully. Thoughtfully, the reversible shape change of 2W-SMPs would provide an alternative option for the above because of controllable actuation behavior and convenient operation procedures.

We preprogrammed C-POA$_3$PCL$_7$ with a double-helix structure as a replacement for the DCB balloon. The axial rotation (positive or negative) of spiral strips results in reversible diameter changes when both ends are fixed by manual welding. Unlike the balloon operation, the diameter changes of the double-helix structure were spontaneous and reversible by simply changing the temperature field in which it is located (Fig. S24, ESI†). When the surface of the double-helix structure was coated with the drug, the vehicle was delivered to the vascular lesion. Then, the diameter of the spiral was expanded to a size similar to the diameter of the blood vessel through heating to T_{high}, resulting in direct contact of the drug with the blood vessel and subsequent absorption by the vessel. After drug release, the diameter was contracted to its initial size through cooling to T_{low}, which made it easier for the vehicle to be recovered to the outside of the body.

A physical model of the above vehicle was made *via* two identical long C-POA$_3$PCL$_7$ samples, as shown in Fig. 4(c). The size of the strips was 40 mm (length) × 3 mm (width) × 0.5 mm (thickness). They were intertwined along the axial direction and physically programmed to be fixed. At the same time, the manual copper ring was fixed at each end of the spiral, and it must be ensured that the rings can rotate freely in the axial direction with the spiral. As a result, the diameter could reversibly change between 2.52 mm and 5.45 mm by heating to 43 °C and cooling to 19 °C. The deformed double-helix structure had a slight non-uniformity at 43 °C. There were two possible reasons. On the one hand, the inherent defects of cross-linked networks made C-POA$_3$PCL$_7$ have a certain thermal response inhomogeneity, which leads to non-cooperative shape changes at local locations of the network.[57] On the other hand, the two ends of the double helix were locked by the copper rings resulting in an unequal stress distribution during the shape changes. The degree of deformation near the end is small, and the degree of deformation far from the end is significant.

Then, we used the C-POA$_3$PCL$_7$ double-helix structure as a drug-carrying vehicle and white floccules as simulated drugs to verify our proposed idea, as shown in Fig. 4(d). The presentation was performed in a semi-enclosed state and the temperature sensor in the picture was used to demonstrate that the real-time temperature obtained was based on the vehicle itself. Due to technical limitations, we were not able to install heating and cooling equipment integrated with the spiral structure. Under ideal conditions, we hoped that future engineering techniques could develop a class of micro-integrated devices to control heating or cooling. Therefore, we need to emphasize that the way of controlling the temperature was not to heat and cool the body directly. As mentioned before, it would be nice to introduce a device that sprayed saline with 43 °C and 19 °C on the vehicle, but this was not the focus of the presentation since the model has a long way to go before it can be applied to real organisms.

In detail, a vascular model with a diameter of about 6 mm was made by a transparent semi-closed glass tube, and the white floccule was initially attached to the vehicle model (Fig. 4(d)-(i)). The vehicle was introduced into the vessel model, and the white floccule did not come into contact with the inner wall of the tube (Fig. 4(d)-(ii)). When the vehicle was heated to 43 °C, the internal stress of C-POA$_3$PCL$_7$ was released; meanwhile, the entropy elasticity of the network drove the spiral structure to rotate axially, increasing the vehicle diameter. The white floccule was extruded and further adhered to the vessel model's inner wall (Fig. 4(d)-(iii)). Then, the vehicle was cooled to 19 °C, and the spiral structure rotated reversely along the axis until its diameter returned to its original state, resulting in its separation from the floccule (Fig. 4(d)-(iv)). This was convenient for the vehicle to be moved out of the model. Finally, we observed the white flocculent left on the wall of the vessel model (Fig. 4(d)-(v)).

As a supplement, the pressure of the C-POA$_3$PCL$_7$ double-helix structure on the inner wall when the diameter increases should also be considered because the high pressure leads to the risk of vessel wall damage. Fig. S25, ESI† shows a flexible mechanical sensor that could detect the pressure on the inner wall of the sensor when the spiral structure expands in real-time. The structure in Fig. 4(c) was tightly wrapped with the above flexible sensor, and then the spiral expansion process was completed from 14 °C to 43 °C. The collected data are shown in Fig. S26, (ESI†); the maximum collectible pressure was 0.9 N, which was lower than the pressure that the vessel's inner wall could bear.[58]

Conclusions

In conclusion, the target networks with an excellent 2W-SME in a narrow response temperature range could be obtained based on the crystallization thermodynamics tunability of the actuation domains. The tunability originated from the cocrystalline (isodimorphic) mechanism formed by POA and PCL crystals, which allowed the synthesized C-POA$_x$PCL$_y$ networks to have two characteristics: (1) the C-POA$_x$PCL$_y$ networks had good crystallizability; (2) the C-POA$_x$PCL$_y$ networks had broadly tunable crystal (melting) transitions. Therefore, tunable T_{high} and remarkable $\Delta\varepsilon_{rev}$ could be achieved by adjusting the components of POA or PCL in the networks. Moreover, multiple T_{high} choices were found for the single network when performed remarkably $\Delta\varepsilon_{rev}$. The difference in non-isothermal crystallization kinetics between POA and PCL crystals resulted in T_{low} also being tunable. Importantly, the networks had less $\Delta\varepsilon_{rev}$ loss by tailoring T_{low} in the appropriate temperature range. As a result, it is feasible to simultaneously tailor T_{high} and T_{low} without highly sacrificing an excellent $\Delta\varepsilon_{rev}$. As the preferred network, C-POA$_3$PCL$_7$ showed more than 17% of $\Delta\varepsilon_{rev}$ in only 24 °C of T-range (between T_{high} of 43 °C and T_{low} of 19 °C). WAXS and SAXS analysis indicated that the reversible actuation

of the networks was credited to the crystallization and melting of the oriented POA crystals, which acted as the actuation and skeleton domains. This also explained the mechanism of how the tunability mentioned above of the actuation domains works. Finally, we discussed the advantages of C-POA_3PCL_7 in being used as potential non-permanently implanted biomedical actuators and designed a medical body micropipe robot with drug release and vehicle recovery functions by referring to DCB technology.

Author contributions

Dequan Chi had charge of methodology, investigation, validation, data curation, formal analysis, and writing – original draft preparation. Yuyan Liu had charge of conceptualization, supervision, funding acquisition, and writing – review & editing. Haoyu Gu had charge of methodology, investigation, and data curation. Jingfeng Wang, Chao Wu, and Ruijie Wang had charge of the methodology and investigation. Zhongjun Cheng, Dongjie Zhang, and Zhimin Xie had charge of the investigation.

Conflicts of interest

The authors declare no conflict of interest.

Acknowledgements

This work was supported by the National Natural Science Foundation of China (grant no. 51573035 and 52273317).

References

1 Y. Xia, Y. He, F. Zhang, Y. Liu and J. Leng, *Adv. Mater.*, 2021, **33**, 2000713.
2 M. D. Hager, S. Bode, C. Weber and U. S. Schubert, *Prog. Polym. Sci.*, 2015, **49–50**, 3–33.
3 Z. Cheng, D. Zhang, X. Luo, H. Lai, Y. Liu and L. Jiang, *Adv. Mater.*, 2020, **33**, 2001718.
4 A. Biswas, V. K. Aswal, P. U. Sastry, D. Rana and P. Maiti, *Macromolecules*, 2016, **49**, 4889–4897.
5 K. Wang, Y. G. Jia, C. Zhao and X. X. Zhu, *Prog. Mater. Sci.*, 2019, **105**, 100572.
6 B. J. Zotzmann, M. Behl, D. Hofmann and A. Lendlein, *Adv. Mater.*, 2010, **22**, 3424–3429.
7 J. Wang, Y. Liu, Y. Yang, J. Wang, H. Kang, H. Yang, D. Zhang, Z. Cheng, Z. Xie, H. Tan and Z. Fan, *Matter*, 2022, **5**, 1042–1055.
8 L. Du, Z.-Y. Xu, C.-J. Fan, G. Xiang, K.-K. Yang and Y.-Z. Wang, *Macromolecules*, 2018, **51**, 705–715.
9 M. Yang, Y. Xu, X. Zhang, H. Bisoyi, P. Xue, Y. Yang, X. Yang, C. Valenzuela, Y. Chen, L. Wang, W. Feng and Q. Li, *Adv. Funct. Mater.*, 2022, **32**, 2201884.
10 K. Wang and X. X. Zhu, *ACS Biomater. Sci. Eng.*, 2018, **4**, 3099–3106.
11 Y. Zhao, Y. Hong, F. Qi, Y. Chi, H. Su and J. Yin, *Adv. Mater.*, 2022, **34**, 2207372.
12 Y. Wu, J. Hu, J. Han, Y. Zhu, H. Huang, J. Lic and B. Tang, *J. Mater. Chem. A*, 2014, **2**, 18816–18822.
13 J. Wang, Z. Tu, H. Zhang, M.-M. Wang, W. Liu and J.-P. Qu, *Macromolecules*, 2022, **55**, 3986–3999.
14 J. Zhang, D. Sun, B. Zhang, Q. Sun, Y. Zhang, S. Liu, Y. Wang, C. Liu, J. Chen, J. Chen, Y. Song and X. Liu, *Mater. Horiz.*, 2022, **9**, 1045–1056.
15 M. Zare, M. P. Prabhakaran, N. Parvin and S. Ramakrishna, *Chem. Eng. J.*, 2019, **374**, 706–720.
16 B. Jin, H. Song, R. Jiang, J. Song, Q. Zhao and T. Xie, *Sci. Adv.*, 2018, **4**, eaao3865.
17 A. Lendlein and O. E. C. Gould, *Nat. Rev. Mater.*, 2019, **4**, 116–133.
18 M. Behl, K. Kratz, J. Zotzmann, U. Nöchel and A. Lendlein, *Adv. Mater.*, 2013, **25**, 4466–4469.
19 G. Chen, B. Jin, Y. Shi, Q. Zhao, Y. Shen and T. Xie, *Adv. Mater.*, 2022, **34**, 2201679.
20 Y. Gao, W. Liu and S. Zhu, *ACS Appl. Mater. Interfaces*, 2017, **9**, 4882–4889.
21 Q. Zhao, H. J. Qi and T. Xie, *Prog. Polym. Sci.*, 2015, **49–50**, 79–120.
22 Z. Xu, L. Li, L. Shi, K.-K. Yang and Y.-Z. Wang, *Macromolecules*, 2022, **55**, 5104–5114.
23 S. Basak and A. Bandyopadhyay, *Adv. Eng. Mater.*, 2022, **24**, 2200257.
24 G. Scalet, *Actuators*, 2020, **9**, 10.
25 J. Zhou, S. A. Turner, S. M. Brosnan, Q. Li, J.-M. Y. Carrillo, D. Nykypanchuk, O. Gang, V. S. Ashby, A. V. Dobrynin and S. S. Sheiko, *Macromolecules*, 2014, **47**, 1768–1776.
26 R. Liang, H. Yu, L. Wang, B. U. Amin, N. Wang, J. Fu, Y. Xing, D. Shen and Z. Ni, *Chem. Mater.*, 2021, **33**, 1190–1200.
27 Y. Meng, J. Jiang and M. Anthamatten, *ACS Macro Lett.*, 2015, **4**, 115–118.
28 M. Farhan, T. Rudolph, U. Nöchel, W. Yan, K. Kratz and A. Lendlein, *ACS Appl. Mater. Interfaces*, 2017, **9**, 33559–33564.
29 A. Lendlein and S. Kelch, *Angew. Chem., Int. Ed.*, 2002, **41**, 2034–2057.
30 H. Song, Z. Fang, B. Jin, P. Pan, Q. Zhao and T. Xie, *ACS Macro Lett.*, 2019, **8**, 682–686.
31 W. Yuan, K. Liu, J. Zhou, L. Ni, G. Shan, Y. Bao and P. Pan, *ACS Macro Lett.*, 2020, **9**, 1325–1331.
32 M. Behl, K. Kratz, U. Noechel, T. Sauter and A. Lendlein, *Proc. Natl. Acad. Sci. U. S. A.*, 2013, **110**, 12555–12559.
33 G. Yang, X. Liu, A. Y. Tok and V. Lipik, *Polym. Chem.*, 2017, **8**, 3833–3840.
34 K. Wang, Y.-G. Jia and X. X. Zhu, *Macromolecules*, 2017, **50**, 8570–8579.
35 N. Inverardi, M. Toselli, G. Scalet, M. Messori, F. Auricchio and S. Pandini, *Macromolecules*, 2022, **55**, 8533–8547.
36 J. Wang, H. Zhang, J. Lei, M. Wu, W. Liu and J.-P. Qu, *Macromolecules*, 2022, **55**, 10113–10123.
37 O. Dolynchuk, I. Kolesov, D. Jehnichen, U. Reuter, H.-J. Radusch and J.-U. Sommer, *Macromolecules*, 2017, **50**, 3841–3854.

38 J. Delaey, P. Dubruel and S. V. Vlierberghe, *Adv. Funct. Mater.*, 2020, **30**, 1909047.
39 R. A. Perez-Camargo, I. Arandia, M. Safari, D. Cavallo, N. Lotti, M. Soccio and A. J. Muller, *Eur. Polym. J.*, 2018, **101**, 233–247.
40 P. Pan, *Prog. Polym. Sci.*, 2009, **34**, 605–640.
41 A. Lendlein, *Proc. Natl. Acad. Sci. U. S. A.*, 2001, **98**, 842–847.
42 M. W. Dewhirst, B. L. Viglianti, M. Lora-Michiels, M. Hanson and P. J. Hoopes, *Int. J. Hyperthermia*, 2003, **19**, 267–294.
43 H. Ang, T. R. Koppara, S. Cassese, J. Ng, M. Joner and N. Foin, *Vasc. Med.*, 2020, **25**, 577–587.
44 Q. Li, J. Zhou, M. Varnoosfaderani, D. Nykypanchuk, O. Gang and S. S. Sheiko, *Macromolecules*, 2016, **49**, 1383–1391.
45 R. A. Pérez-Camargoa, I. Arandiaa, M. Safaria, D. Cavallob, N. Lottic, M. Soccioc and A. J. Müllera, *Eur. Polym. J.*, 2018, **101**, 233–247.
46 J. Mark, *Polymer Data Handbook*, Oxford University Press, New York, 1999.
47 W. Yuan, J. Zhou, K. Liu, X. Li, W. Xu, H. Song, G. Shan, Y. Bao, Q. Zhao and P. Pan, *ACS Macro Lett.*, 2020, **9**, 588–594.
48 X. Li and Z. Qiu, *Macromol. Res.*, 2015, **23**, 678–685.
49 R. A. Pérez-Camargo, D. Cavallo, T. Debuissy, E. Pollet, L. Avérous and A. J. Müller, *Macromolecules*, 2017, **50**, 597–608.
50 M. Huang, X. Dong, L. Wang, J. Zhao, G. Liu and D. Wang, *RSC Adv.*, 2014, **4**, 55483–55494.
51 G. Weng, J. Bao, Y. Xu and Z. Chen, *J. Polym. Res.*, 2013, **20**, 104.
52 M. W. Dewhirst, B. L. Viglianti, M. Lora-Michiels, M. Hanson and P. J. Hoopes, *Int. J. Hyperthermia*, 2003, **19**, 267–294.
53 W. J. Mohr, K. Jenabzadeh and D. H. Ahrenholz, *Hand Clin.*, 2009, **25**, 481–496.
54 Q. Zhao, J. Wang, Y. Wang, H. Cui and X. Du, *Natl. Sci. Rev.*, 2020, **7**, 629.
55 Q. Zhao, J. Wang, H. Cui, H. Chen, Y. Wang and X. Du, *Adv. Funct. Mater.*, 2018, **28**, 1801027.
56 C. Lin, J. Lv, Y. Li, F. Zhang, J. Li, Y. Liu, L. Liu and J. Leng, *Adv. Funct. Mater.*, 2019, **29**, 1906569.
57 X. Huang, S. Nakagawa, X. Li, M. Shibayama and N. Yoshie, *Angew. Chem., Int. Ed.*, 2020, **59**, 9646–9652.
58 A. V. Kamenskiy, Y. A. Dzenis, C. Lomneth and J. MacTaggart, *Biomech. Model. Mechanobiol.*, 2014, **13**, 1341–1359.

